Emergent quasicrystal in fermionic superradiance

Bo-Hao Wu,[1] Xin-Xin Yang,[1] Wei Zhang,[1,2,3,*] and Yu Chen[4,†]

[1]School of Physics and Key Laboratory of Quantum State Construction and Manipulation (Ministry of Education), Renmin University of China, Beijing 100872, China

[2]Beijing Academy of Quantum Information Sciences, Beijing 100193, China

[3]Beijing Key Laboratory of Opto-electronic Functional Materials and Micro-nano Devices, Renmin University of China, Beijing 100872, China

[4]Graduate School of China Academy of Engineering Physics, Beijing 100193, China

(Received 17 August 2023; revised 21 February 2024; accepted 3 January 2025; published 15 January 2025)

Quasicrystal is state of matter with multiple crystalline orders, displaying a short-range density-wave order and a long-range disorder. As an exotic state lying in between crystals and Anderson insulators, its dynamical formation is little discussed. Here, we study the emergence of quasicrystalline order in fermionic superradiance, where Fermi statistics plays a crucial role, being distinct from its bosonic counterpart where interaction is the stabilizer. Owing to quasicrystalline orders, there exist multiple energy gaps opening at different quasicrystalline order strength, which can modify the density of states in excitation spectrum. As a result, the effective ground-state energy is strongly modified and the superradiant quasicrystal transition becomes first order and density dependent. This new mechanism leads to a linear V-shape kink of the fermionic superradiance transition line near a filling which uniquely relates to the quasicrystalline order. Our findings demonstrate that quasicrystal can be realized in fermionic superradiance as a result of Fermi statistics and be verified by characteristic density-dependent phenomena.

DOI: 10.1103/PhysRevResearch.7.013056

I. INTRODUCTION

Quasicrystals (QC) are originally discovered in materials with forbidden crystallographically symmetry such as five-fold rotation symmetry [1,2], and are later understood as a result of incommensurate crystalline orders [3–5]. After being studied intensively for serval decades [6], there is still a lot of debate on the formation and stability mechanism of QC, especially for the role of entropy in the context of a thermodynamic phase transition [7]. There is little discussion on the formation of QC as a quantum phase transition, where new mechanisms other than entropy may play a central role. Compared to conventional solid-state systems, cold atomic gases in optical lattices serve as a more controllable platform to study the emergence and property of density orders [8]. In incommensurate optical lattices, the competition between QC and localization is studied [9–16]. However, the QC transition therein is induced by the externally imposed background potentials only, while the dynamical feedback and spontaneous emergence of atomic orders are missing.

With the help of recent progresses in cavity quantum electrodynamics, in particular, the pursuit of strong interaction between atoms and cavity photons, steady-state superradiance (SR) is realized accompanied with a self-organized density order of atoms [17–21]. With the aid of advanced laser cooling techniques, this hybrid system offers an ideal platform for studying QC ordering as a quantum phase transition at a temperature well below quantum degeneracy [22,23]. Previous studies investigate the single-particle dynamics of bosonic atoms in emergent incommensurate lattices and find a Lévy walk [24]. Further, an enhancement of Anderson insulators and an interaction-stabilized QC with spontaneous eightfold rotation symmetry are found within Bose-Einstein condensate (BEC) in emergent lattices [25,26]. While most existing works focus on Bose gases only, one would wonder whether new mechanisms and features can be found in the formation of Fermi QC, especially when crucial effects of Fermi statistics in SR are suggested for degenerate Fermi gases [27–29] and evidences are observed in recent experiments [30–34].

In this article, we study the SR transition of a one-dimensional (1D) spinless Fermi gas in a cavity with an incommensurate dipolar lattice, as depicted in Fig. 1(a). We find that the SR transition and the spontaneous formation of QC ordering are strongly density dependent [Fig. 1(b)], with dips of critical pumping at different particle fillings. Such a characteristic phase diagram is a direct consequence of combining effects of Fermi surface (FS) nesting and indirect resonance (IR), where FS nesting is more crystalline order related and IR effect is uniquely connected to QC ordering. The mechanism of IR is illustrated in Fig. 1(c). A resonance

*Contact author: wzhangl@ruc.edu.cn
†Contact author: ychen@gscaep.ac.cn

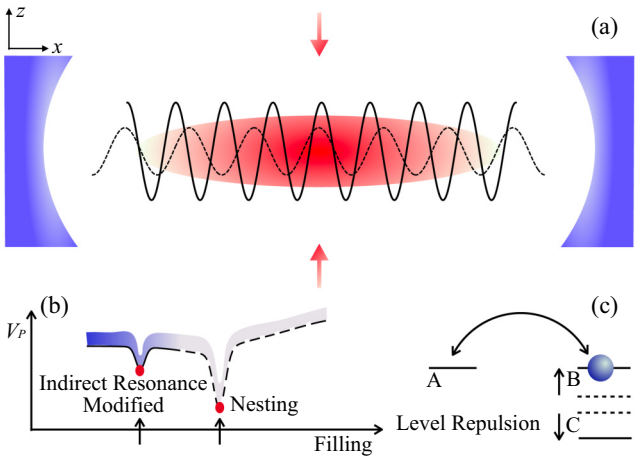

FIG. 1. (a) A 1D Fermi gas placed in a cavity with an incommensurate dipolar lattice along the $\hat{x}$ direction, and driven by pumping field along the $\hat{z}$ direction. (b) Schematic phase diagram of the QC SR transition showing the critical pumping strength V_p as a function of filling. The solid and dashed lines denote first- and second-order transitions, respectively. The color above the line denotes the mean cavity photon number after transition with dark (light) color representing large (small) photon number. The FS nesting and IR effects are shown as dips. (c) Mechanism of IR effect, a resonance by level repulsion.

can take place between two levels (A and B), where the energy of B level is shifted by level repulsion from a third level (C) due to the potential of QC ordering, and lead to a gap opening. This phenomenon is similar to the scheme of variable-range hopping in interacting disordered systems [35–37], where two off-resonant localized states can reach resonance by the absorption of a phonon. We show how the extra gaps induced by IR, together with Fermi statistics, become the major reason for QC ordering in fermionic SR. We also find that the kink of critical pumping related to the IR effect and the linear V-shape transition line nearby are smoking-gun evidences of this mechanism, as explained by a phenomenological theory and verified by numerical simulation using experimentally relevant parameters.

II. MODEL AND MEAN FIELD THEORY

We consider a 1D spinless Fermi gas placed in a high-finesse cavity. The Fermi gas is assumed to be aligned along the $\hat{x}$ direction, which is also the cavity direction as shown in Fig. 1(a). The system is subjected to two counterpropagating dipolar laser beams along the $\hat{x}$ direction, polarized in the $\hat{y}$ direction, and two pumping lasers along the $\hat{z}$ direction, polarized in the $\hat{y}$ direction. Both the pumping frequency and the cavity frequency are far detuned from the atomic excitation energy. By using a standard rotating-wave approximation, we obtain the Hamiltonian ($\hbar = k_B = 1$)

$$\hat{H} = \int dx \hat{\Psi}^\dagger(x)\hat{H}_0\hat{\Psi}(x) - \Delta_c \hat{a}^\dagger\hat{a}, \tag{1}$$

$$\hat{H}_0 = \hat{H}_{\rm at} + \eta(x)(\hat{a}^\dagger + \hat{a}) + U(x)\hat{a}^\dagger\hat{a}, \tag{2}$$

$$\hat{H}_{\rm at} = -\frac{\partial_x^2}{2m} - \mu + V_d(x), \tag{3}$$

where $\hat{\Psi}(x)$ is the field operator of fermions with chemical potential μ, $\hat{a}$ is the cavity field operator, and Δ_c is the cavity field detuning. The dipolar potential is $V_d(x) = V_d\cos^2(k_d x)$ and the cavity field self-energy potential is $U(x) = U_0\cos^2(k_c x)$, with corresponding wave numbers k_d and k_c. The depth of $U_0 = g_0^2/\Delta_{\rm AC}$ is determined by the atom-cavity coupling strength g_0 and the AC Stark shift $\Delta_{\rm AC}$. The interference lattice between the pumping field and the cavity field is $\eta(x) = \eta_0\cos(k_c x)$, where $\eta_0 = \Omega_p g_0/\Delta_{\rm AC}$ with Ω_p the Rabi frequency of the pumping field. The pumping field strength is $V_p = \Omega_p^2/\Delta_{\rm AC}$ and satisfies $V_p = \eta_0^2/U_0$. The superradiant transition could be driven by adjusting V_p. In the following discussion, we define the recoil energy $E_R = k_d^2/2m$ as the energy unit and choose $k_c/k_d = 2(\sqrt{2}-1)$ as a particular example.

We adopt the mean field approach and assume that $\alpha \equiv \langle\hat{a}\rangle$ at the steady state, where $\langle\cdot\rangle \equiv {\rm tr}(\cdot\hat{\rho}_{\rm st})$ represents an ensemble average over the steady-state density matrix $\hat{\rho}_{\rm st} = e^{-\beta\hat{\mathcal{H}}_{0,\alpha}}/\mathcal{Z}_\alpha \otimes |\alpha\rangle\langle\alpha|$ with $\beta = 1/T$ the inverse temperature. Here, $|\alpha\rangle$ is the coherent state of the cavity photon, $\mathcal{Z}_\alpha = {\rm Tr}(e^{-\beta\hat{\mathcal{H}}_{0,\alpha}})$, and $\hat{\mathcal{H}}_{0,\alpha} = \langle\alpha|\int dx\hat{\Psi}^\dagger(x)\hat{H}_0\hat{\Psi}(x)|\alpha\rangle$. This assumption is justified more comprehensively by the Keldysh Green's function method [38]. The dynamical equation for the cavity field then follows the steady equation $i\partial_t\alpha = \langle[\hat{a},\hat{H}]\rangle - i\kappa\alpha$, which can be written as

$$i\partial_t\alpha = \partial_{\alpha^*}\mathcal{F}_\alpha - i\kappa\alpha. \tag{4}$$

Here, κ is the cavity decay rate and the free energy is given by $\mathcal{F}_\alpha \equiv -T\log\mathcal{Z}_\alpha - \Delta_c\alpha^*\alpha$. One can check $-T\partial\log\mathcal{Z}_\alpha/\partial\alpha^* = \eta_0\Theta + U_0\mathcal{B}\alpha$, where $\Theta = {\rm Tr}(\hat{\Theta}e^{-\beta\hat{\mathcal{H}}_{0,\alpha}})/\mathcal{Z}_\alpha$ is the fermionic density order with $\hat{\Theta} = \int dx\hat{\Psi}^\dagger(x)\eta(x)\hat{\Psi}(x)/\eta_0$, and $\mathcal{B} = {\rm Tr}(\hat{\mathcal{B}}e^{-\beta\hat{\mathcal{H}}_{0,\alpha}})/\mathcal{Z}_\alpha$ is another density order with $\hat{\mathcal{B}} \equiv \int dx\hat{\Psi}^\dagger(x)U(x)\hat{\Psi}(x)/U_0$. For simplicity, we assume that the temperature of atoms is zero, and $\mathcal{F}_\alpha$ is just the ground-state energy E_α.

For a steady state, we have $\partial_t\alpha = 0$, which translates to

$$\alpha = \frac{\eta_0\Theta}{\tilde{\Delta}_c + i\kappa}, \tag{5}$$

with $\tilde{\Delta}_c \equiv \Delta_c - U_0\mathcal{B} \approx \Delta_c - U_0 N_{\rm at}/2$ and $N_{\rm at}$ the atom number. This steady-state equation can in principle be solved numerically, but the outcome may be difficult to interpret to identify the underlying physics. Instead, we adopt an equivalent method to minimize the energy E_α. First of all, we notice that the density order Θ is real. Therefore, the phase of the steady-state cavity field is determined by the ratio of $\tilde{\Delta}_c$ and κ. Secondly, although there is another density order $\mathcal{B}$ controlled by the U_0 term and $\tilde{\Delta}_c$ is in general not a constant, for simplicity we can assume a large $\tilde{\Delta}_c$ such that the phase of the cavity field is approximately a constant. Under this condition, the minimization of E_α with respect to α is equivalent to solving the steady-state equation.

To obtain the ground-state energy of the atomic field for a virtually condensed α, we need to calculate the eigenvalues of $\hat{H}_0(\alpha) = \langle\alpha|\hat{H}_0|\alpha\rangle$. By denoting the eigenvalue of $\hat{H}_0(\alpha)$ as $\varepsilon_{n,\alpha}$, such that $\hat{H}_0(\alpha)\phi_{n,\alpha} = \varepsilon_{n,\alpha}\phi_{n,\alpha}$, we obtain the ground-

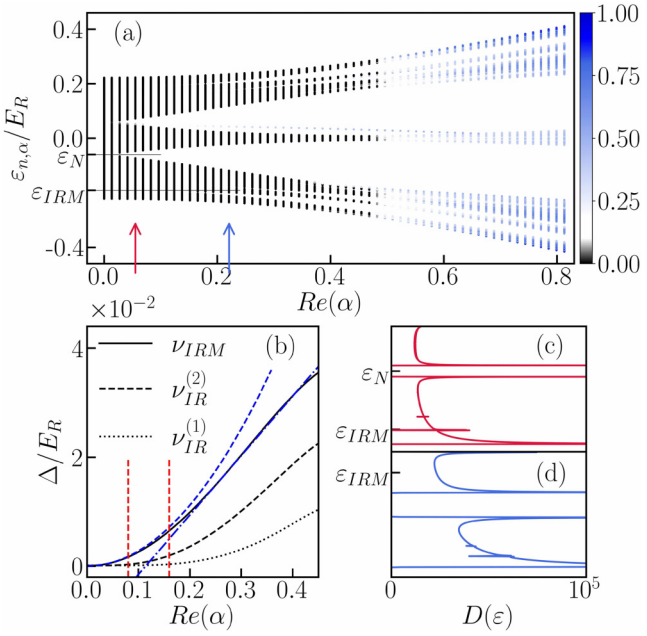

FIG. 2. (a) The single-particle spectrum of $\hat{H}_0$ as a function of Re(α) and the IPR of all eigenstates (false color). (b) The gap width Δ/E_R as a function of Re(α) at different filling factors $\nu_{\rm IRM} = 1 - k_c/k_d$, $\nu_{\rm IR}^{(1)} = 2 - 2k_c/k_d$, and $\nu_{\rm IR}^{(2)} = 3k_c/2k_d - 1$. The red dashed lines correspond to IR gap-opened points. The blue dashed and dot-dashed lines are quadratic and linear fits of the dispersion of $\nu_{\rm IRM}$, respectively. (c and d) The DOS around nesting and IRM fillings with different Re(α), labeled by red and blue arrows in (a). Here, $V_d/E_R = 3$, $V_p/E_R = -7.469$, $U_0/E_R = -0.01$, $\Delta_c/E_R N_{\rm at} = -0.155$, $\kappa/E_R N_{\rm at} = 0.0075$, and $N = 4000$ (N is the system size).

state energy

$$E_\alpha = \sum_n \varepsilon_{n,\alpha}\theta(\varepsilon_F - \varepsilon_{n,\alpha}) - \Delta_c\alpha^*\alpha, \tag{6}$$

where $\theta(x)$ is the Heaviside step function and ε_F is the Fermi energy fixed by the filling fraction defined in the thermodynamic limit. The expression above is composed by two contributions, including the vacuum energy $E_{\rm vac} = \varepsilon_{0,\alpha}N_{at} - \Delta_c\alpha^*\alpha$ and the occupation energy $E_{\rm occ} = \sum_n(\varepsilon_{n,\alpha} - \varepsilon_{0,\alpha})\theta(\varepsilon_F - \varepsilon_{n,\alpha})$. Fermi statistics and the consequent density-dependent effect are mainly manifested in $E_{\rm occ}$.

III. NESTING AND INDIRECT RESONANCE EFFECTS

Next, we present the results of minimization of E_α for the 1D Fermi gas under open boundary conditions. We first show some numerical results, then introduce an effective theory to explain the nesting and IR effects. For numerical treatment, we first solve the Bloch states $|k\rangle$ as the eigenstates of $\hat{H}_{\rm at}$ with only the dipolar lattice $V_d(x)$. By focusing on the lowest band, we construct the Wannier basis $|j\rangle = \sum_k e^{ikj}|k\rangle$ using Bloch states $|k\rangle$ with $k \in [-k_d, k_d)$ in the first Brillouin zone. The Hamiltonian $\hat{H}_0(\alpha)$ can be expanded in the basis of $|j\rangle$ with a finite-size cutoff and then solved by numerical diagonalization. The numerical details are summarized in Appendix A.

In Fig. 2(a), we show the single-particle spectrum of $\hat{H}_0$ as a function of Re(α), which characterizes the depth of the superradiant lattice. The results present several apparent gaps at different fillings (thin solid lines). Firstly, one can see a gap opening at zero cavity field $\alpha = 0$ at a special energy $\varepsilon_{\rm N}$. The filling of this energy is $\nu_{\rm N} = k_c/2k_d$, at which the states $|\pm k_c/2\rangle$ are resonant. This is addressed as a FS nesting effect, which leads to a direct resonance gap that is proportional to $|\alpha|$. Besides, other gaps can also be seen at filling factors $\nu_{\rm IRM} = 1 - k_c/k_d$, $\nu_{\rm IR}^{(1)} = 2 - 2k_c/k_d$, and $\nu_{\rm IR}^{(2)} = 3k_c/2k_d - 1$, and the gap widths as functions of Re(α) are given in Fig. 2(b).

For the gaps at $\nu_{\rm IR}^{(1)} = 2 - 2k_c/k_d$ and $\nu_{\rm IR}^{(2)} = 3k_c/2k_d - 1$, one can clearly find that these gaps are opened at finite $|\alpha|$ [red dashed lines in Fig. 2(b)], and are classified as IR gaps. Take $\nu_{\rm IR}^{(1)}$ as an example. Originally, $|2k_d - 2k_c\rangle$ and $|2k_d - 3k_c\rangle$ are close to each other but not resonant. The η term of the Hamiltonian gives a strong repulsion between these two levels and one level becomes resonant with $|k_d\rangle$, causing an IR gap opening. A similar phenomenon is also observed for filling $\nu_{\rm IR}^{(2)} = 3k_c/2k_d - 1$. In addition, the newly opened IR gaps can modify the existing direct resonance gaps as a result of level repulsion, that is, every new gap will compress the existing gaps. Specifically, at the filling $\nu_{\rm IRM} = 1 - k_c/k_d$ (IRM stands for IR modified), a gap is present for arbitrarily small $\alpha = 0$ at an energy $\varepsilon_{\rm IRM}$, owing to the direct resonance process with an intensity U_0 and a $2k_c$ momentum transfer. Thus, this gap should be proportional to $|\alpha|^2$ [blue dashed line in Fig. 2(b)], at least for small $|\alpha|$. However, when an IR gap opens at a finite $|\alpha|$, the level repulsion effect will alter the $|\alpha|^2$ behavior of the direct resonance gaps, and cause a linear dependence [blue dot-dashed line in Fig. 2(b)] on the cavity condensation strength.

IV. PHENOMENOLOGICAL THEORY AND PHASE DIAGRAM

To characterize the SR transitions, in particular, around the nesting and IRM fillings, next we derive a phenomenological theory. To begin with, we notice that the density of states (DOS) presents van Hove singularities and diverges as $|\varepsilon_{\rm ed} - \varepsilon|^{-\frac{1}{2}}$ around the gap edge $\varepsilon_{\rm ed}$, for gaps opened by either FS nesting effect [Fig. 2(c)] or IR effect [Fig. 2(d)]. Here, we set α to be real for simplicity.

For the case of the nesting gap, we assume a single-particle dispersion $\varepsilon_k = \tilde{\varepsilon}_{\rm N} - \sqrt{(k^2/2m^* - \tilde{\varepsilon}_{\rm N})^2 + 4\eta^2\alpha^2}$ for the band below the nesting filling, where m^* is the effective mass, $\tilde{\varepsilon}_{\rm N} = \varepsilon_{\rm N} - \varepsilon_{n=0,\alpha=0}$ is the Fermi energy at $\nu_{\rm N}$ shifted by the band bottom before the SR transition ($\alpha = 0$), and $2|\eta\alpha|$ is the gap width. The gap edge $\varepsilon_{\rm ed}$ is $\tilde{\varepsilon} - 2|\eta\alpha|$. The DOS then reads

$$D_\alpha(\varepsilon) = \frac{D_0}{\sqrt{\tilde{\varepsilon}_{\rm N} - \sqrt{\Delta\varepsilon^2 - 4\eta^2\alpha^2}}} \frac{|\Delta\varepsilon|}{\sqrt{\Delta\varepsilon^2 - 4\eta^2\alpha^2}}, \tag{7}$$

where $\Delta\varepsilon = \tilde{\varepsilon}_{\rm N} - \varepsilon$. Notice that this simple form of dispersion can correctly describe the divergence of DOS near the gap edge, and qualitatively capture the overall shape of the actual dispersion down to the single-particle ground state $\varepsilon_{g0} = \tilde{\varepsilon}_{\rm N} - \sqrt{\tilde{\varepsilon}_{\rm N}^2 + 4\eta^2\alpha^2}$. The prefactor D_0 can be solved via the number constraint of total available states $N_0 = \int_{\varepsilon_{g0}}^{\varepsilon_{ed}} d\varepsilon D_\alpha(\varepsilon)$, and is quantitatively affected by the details of dispersion.

To calculate the ground-state energy of the system $E_g(\alpha) = E_{\rm vac}(\alpha) + E_{\rm occ}(\alpha)$, we first assume without loss of generality

that the shift of the band bottom $E_{\rm vac}(\alpha) \approx \delta\alpha^2$ for small α, owing to the Z_2 symmetry of the SR transition as discussed in Appendix B. The shift is a joint effect of gap opening and cavity detuning, and acquires a positive prefactor δ as confirmed by numerical calculation. On the other hand, the occupation energy $E_{\rm occ}(\alpha) = \int_{\varepsilon_{g0}}^{\mu} d\varepsilon \varepsilon D_\alpha(\varepsilon)$ can be calculated by summing over all states below the chemical potential μ determined by the filling. By denoting the deviation from the perfect nesting filling $\nu_{\rm N}$ as $\tilde{\nu}_{\rm N} = 1 - \nu/\nu_{\rm N}$, we get $\mu \approx \tilde{\varepsilon}_{\rm N}[1 - 2\sqrt{\tilde{\nu}_{\rm N}^2 + (\eta\alpha/\tilde{\varepsilon}_{\rm N})^2}]$ for small $\tilde{\nu}_{\rm N}$, and

$$E_g^{\rm N}(\alpha) = \delta\alpha^2 - N_0\tilde{\varepsilon}_{\rm N}\int_{\tilde{\nu}_{\rm N}}^{1} dx \sqrt{x^2(2-x)^2 + \frac{4\eta^2\alpha^2}{\tilde{\varepsilon}_{\rm N}^2}}. \quad (8)$$

A phase transition occurs when the overall coefficient of the α^2 term changes sign. For a system at $\nu_{\rm N}$, the leading order of the integral above is $\alpha^2 \log|\alpha|$, hence guarantees a divergent coefficient of the α^2 term for small α. This observation explains the nesting effect of the SR transition, and explains why the critical pumping strength increases rapidly when ν moves away from $\nu_{\rm N}$. Detailed calculation can be found in Appendix D.

For a system at the IRM filling $\nu_{\rm IRM}$, the DOS follows a similar form as for the nesting gap

$$D'_\alpha(\varepsilon) = \frac{D'_0}{\sqrt{\tilde{\varepsilon}_{\rm R} - \sqrt{\Delta\varepsilon'^2 - \Delta_{\rm IRM}^2(\alpha)}}} \frac{|\Delta\varepsilon'|}{\sqrt{\Delta\varepsilon'^2 - \Delta_{\rm IRM}^2(\alpha)}}, \quad (9)$$

with $\tilde{\varepsilon}_{\rm R} = \sqrt{\tilde{\varepsilon}_{\rm N}^2 + 4\eta^2\alpha^2} - \sqrt{(\tilde{\varepsilon}_{\rm N} - \tilde{\varepsilon}_{\rm IRM})^2 + 4\eta^2\alpha^2}$, $\Delta\varepsilon' = \tilde{\varepsilon}_{\rm R} - \varepsilon$, $\tilde{\varepsilon}_{\rm IRM} = \varepsilon_{\rm IRM} - \varepsilon_{0,0}$, and $\Delta_{\rm IRM}(\alpha)$ the IRM gap width as a function of α. D'_0 is determined by requiring $\int_{\tilde{\varepsilon}_{\rm IRM} - \sqrt{\tilde{\varepsilon}_{\rm IRM}^2 + \Delta_{\rm IRM}^2}}^{\tilde{\varepsilon}_{\rm R} - \Delta_{\rm IRM}} D'_\alpha(\varepsilon)d\varepsilon = N'_0 = N_0\nu_{\rm IRM}/\nu_{\rm N}$. Here, $\tilde{\varepsilon}_{\rm R} - \Delta_{\rm IRM}$ is the upper band-edge energy and $\tilde{\varepsilon}_{\rm IRM} - \sqrt{\tilde{\varepsilon}_{\rm IRM}^2 + \Delta_{\rm IRM}^2}$ is the single-particle ground-state energy. The DOS ensures two van Hove singularities on the band edges if the gaps are open. A similar calculation gives (see Appendix D for details)

$$E_g^{\rm IR}(\alpha) = E_{\rm vac}(\alpha) - N'_0\tilde{\varepsilon}_{\rm R}\int_{\tilde{\nu}_{\rm IRM}}^{1} dx \times \sqrt{x^2(2-x)^2 + \frac{\Delta_{\rm IRM}^2(\alpha)}{\tilde{\varepsilon}_{\rm R}^2}}, \quad (10)$$

with $\tilde{\nu}_{\rm IRM} = 1 - \nu/\nu_{\rm IRM}$. The key difference of the IRM gap is that $\Delta_{\rm IRM}$ is quadratically dependent on α for small α, as can be read from the numerical diagonalization. The SR transition can only take place for a finite $\alpha = \alpha_c$, such that the minima of E_g at $\alpha = 0$ and $|\alpha_c|$ become degenerate. When the filling is slightly deviated from $\nu_{\rm IRM}$, a perturbation analysis given in Appendix E shows that the critical pumping strength of the SR transition is linearly dependent on filling, leading to a kink structure.

To further explore the filling ν in between $\nu_{\rm IRM}$ and $\nu_{\rm N}$, we need to consider both the influence of the direct resonance and IR effect on the DOS. As shown in Appendix E, a reasonable

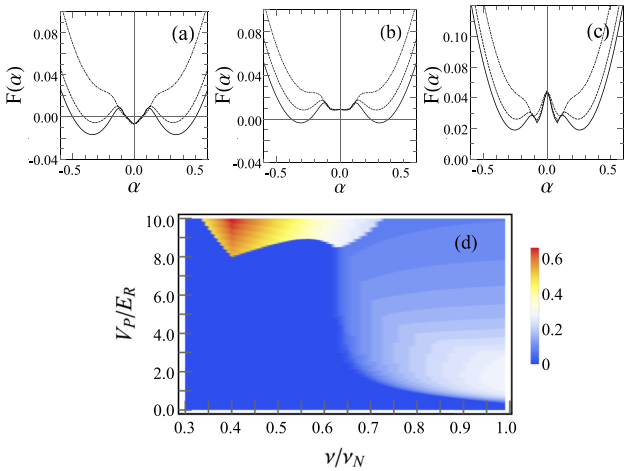

FIG. 3. The free energy $F(\alpha)$ as a function of α for (a) $\nu/\nu_{\rm N} = 0.6$, (b) 0.625, and (c) 0.68, obtained using the phenomenological model with effective DOS. In each panel, the dot-dashed, dashed, and solid curves (from top to bottom) represent the results for pumping strengths V_p in ascending order. One can observe a first-order SR transition in (a) and a first-order transition within the SR phase in (c). A critical case where the SR transition changes from first order to second order is shown in (b). (d) Phase diagram obtained from the phenomenological theory, with the order parameter α depicted by false color. A kink at $\nu_{\rm IRM}/\nu_{\rm N} = 0.4$ and a first-order-to-second-order transition at $\nu/\nu_{\rm N} = 0.625$ are clearly witnessed.

fitting of the DOS is

$$D''_\alpha(\varepsilon) = \frac{D''_0|\Delta\varepsilon''|}{\sqrt{\Delta\varepsilon''^2 - \Delta_{\rm IRM}^2(\alpha)}} \frac{|\Delta\varepsilon|}{\sqrt{\Delta\varepsilon^2 - 4\eta^2\alpha^2}}, \quad (11)$$

where $\Delta\varepsilon'' = \varepsilon - \tilde{\varepsilon}_d$, $\Delta\varepsilon = \varepsilon - \tilde{\varepsilon}_u$, and $\tilde{\varepsilon}_d = \tilde{\varepsilon}_{\rm N} - \sqrt{(\varepsilon_{\rm N} - \varepsilon_{\rm IRM})^2 + 4\eta^2\alpha^2}$ and $\tilde{\varepsilon}_u = \tilde{\varepsilon}_{\rm N} + \Delta_{\rm IRM}$ are lower and upper bounds of the edge energy, respectively. The extra $\Delta_{\rm IRM}$ shift in $\tilde{\varepsilon}_u$ ensures the upper bound being always larger than the lower bound. The value of D''_0 can be fixed by requiring $\int_{\tilde{\varepsilon}_d + \Delta_{\rm IRM}}^{\tilde{\varepsilon}_u - 2\eta\alpha} D''_\alpha(\varepsilon)d\varepsilon = N_0 - N'_0$. The two van Hove singularities are kept by this approximation. The chemical potential μ can be determined by $\int_{\tilde{\varepsilon}_d + \Delta_{\rm IRM}}^{\mu} D''_\alpha(\varepsilon)d\varepsilon = N - N'_0$. The ground-state energy can then be accessed as $E_g(\alpha) = E_g^{\rm IR}(\alpha)|_{\tilde{\nu}_{\rm IRM}=0} + \int_{\tilde{\varepsilon}_d + \Delta_{\rm IRM}}^{\mu} D''_\alpha(\varepsilon)\varepsilon d\varepsilon$.

As an example, we take $\delta/N_0\tilde{\varepsilon}_{\rm N} = 0.5$ and $\nu_{\rm IRM} = 0.4\nu_{\rm N}$. Phenomenologically we employ $\Delta_{\rm IRM} = 0.2\Theta(|\eta\alpha| - P_c)(|\eta\alpha| - P_c)$ with $P_c/N_0\tilde{\varepsilon}_{\rm N} = 0.8$ to mimic the linear gap with finite critical pumping strength. The ground-state energy as a function of α for different fillings $\nu/\nu_{\rm N} = 0.6$, 0.625, and 0.68 are depicted in Figs. 3(a), 3(b), and 3(c), respectively. By varying the pumping strength, the energy curves show a first-order transition from N to SR phase for $\nu/\nu_{\rm N} = 0.6$, and a first-order transition within the SR phase at $\nu/\nu_{\rm N} = 0.68$. The phase diagram is given in Fig. 3(d) based on our phenomenological theory. A clear kink by IR effect in shown and a first-order-to-second-order transition is found by changing filling faction.

The above characteristic features of QC in fermionic SR obtained from the effective DOS can be verified by numerical simulation. The ground-state energy density $E_g(\alpha)/E_R N_{\rm at}$ as

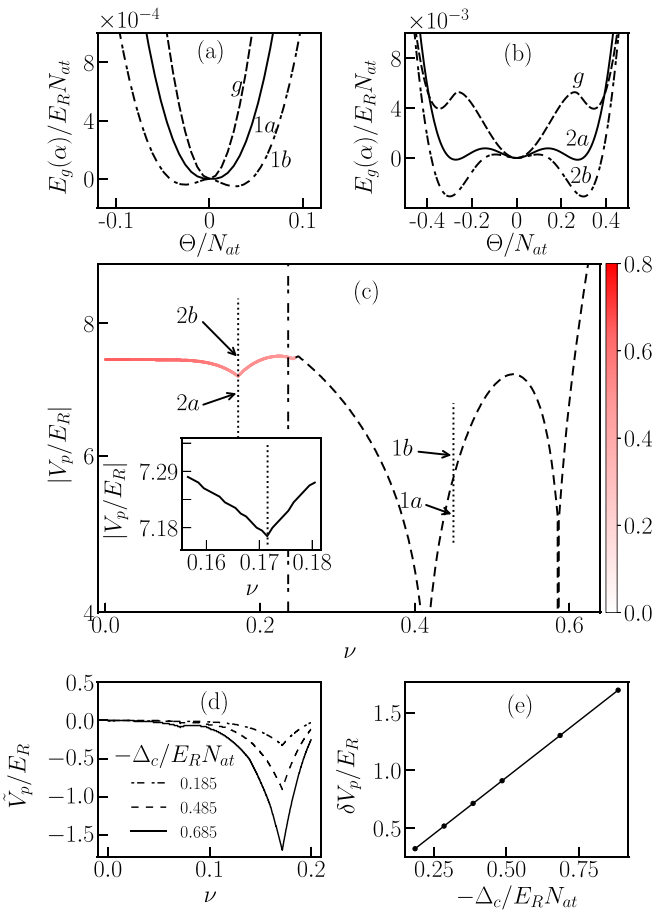

FIG. 4. (a and b) The ground-state energy density $E_g(\alpha)/E_R N_{\rm at}$ as a function of the fermion density order $\Theta/N_{\rm at}$ at positions marked as 1a, 1b, 2a, and 2b in (c). The dashed lines labeled by g denote the vacuum energy densities $E_{\rm vac}/E_R N_{\rm at}$ at phase boundary. (c) The phase diagram in terms of filling factor ν and critical pumping field strength V_p/E_R. The solid (dashed) line represents the first-order (second-order) phase boundary and the false color at first-order phase boundary denotes the cavity field $|\alpha|$. The dot-dashed line denotes the boundary between AL phase and QC phase. The inset shows the kink structure with a linear V shape around $\nu = \nu_{\rm IRM}$. The kink depth is about $0.11E_R$. Here, $V_d/E_R = 3$, $U_0/E_R = -0.01$, $\Delta_c/E_R N_{\rm at} = -0.155$, $\kappa/E_R N_{\rm at} = 0.0075$, and $N = 4000$. In (d), we show the critical pumping strength as a function of filling fraction for different cavity detune Δ_c. $V_p(\nu = 0)$ are taken as 0 for reference. In (e), we show the kink depth $\delta V_p \equiv V_p(\nu_{\rm IRM}) - V_p(0)$ as a function of cavity detune Δ_c and we find a linear dependence in kink depth and the cavity detune. When $\Delta_c/E_R N_{\rm at} = 0.8$, the kink depth can be $1.5E_R$. The relative coefficient of the linear fit is 0.999 964.

a function of the fermion density order $\Theta/N_{\rm at}$ at representative points near $\nu_{\rm N}$ and $\nu_{\rm IRM}$ are displayed in Figs. 4(a) and 4(b), showing typical behavior of second-order and first-order phase transitions, respectively. The phase diagrams for different filling factors and critical pumping field strengths are given in Fig. 4(c). The normal phase with $\alpha = 0$ (bottom) is separated from the SR phase (top) by either a second-order transition (dashed line) for large filling or a first-order transition (solid line) for small filling. The cavity field $|\alpha|$ (false color) is finite at the first-order transition and zero at the second-order transition. For both cases, a finite size scaling is conducted and summarized in Appendix B, and the results shown here are the thermodynamic limit. Three dips with minimal critical pumping are observed at $\nu_{\rm IRM} = 1 - k_c/k_d$ and $\nu_{\rm N} = k_c/2k_d$, $1 - k_c/2k_d$. In the inset, we zoom around $\nu = \nu_{\rm IRM}$ to show the kink structure with a linear V shape. Further, we calculate the inverse participation ratio (IPR) of all occupied states defined in Appendix C right after the superradiant transition, and find that the system is in Anderson localization (AL) phase for $\nu < \nu_{\rm AL}$ and quasi-crystal phase for $\nu > \nu_{\rm AL}$. The critical filling $\nu_{\rm AL}$ is marked as a dot-dashed line in Fig. 4(c).

To evaluate the experimental feasibility to observe the IR effect, we define the kink depth of phase boundary as the deviation of critical pumping strength between $\nu = 0$ and $\nu = \nu_{\rm IRM}$

$$\delta V_p = V_p(\nu_{\rm IRM}) - V_p(0), \tag{12}$$

where $V_p(\nu)$ is the critical pumping strength at filling factor ν. The deviation as a function of cavity field detuning is shown in Figs. 4(d) and 4(e). We find that the IR effect is more significant with a deeper kink for large cavity detuning, and should be able to resolve under typical experimental conditions.

V. SUMMARY

To summarize, we study the superradiance transition of a one-dimensional Fermi gas coupled to an incommensurate cavity. We find spontaneously emerged quasicrystal order showing strong density dependence due to Fermi surface nesting effect and IR effect. The IR effect makes superradiance transition highly sensitive to density, resulting in a minimal critical pumping at a specific filling $\nu = \nu_{\rm IRM}$, around which the critical pumping strength depends linearly on the filling and presents a V-shape kink in the phase diagram. This unique characteristic can act as smoking-gun evidence for the IR effect. These phenomena are generally applicable to other quasicrystal systems and are expected to be presented in higher-dimensional systems as well. All of our predictions can be tested in future experiments of ultracold Fermi gases in optical cavities.

ACKNOWLEDGMENTS

This work is supported by the National Key R&D Program of China (Grant No. 2022YFA1405300), the National Natural Science Foundation of China (Grants No. 11734010, No. 12074428, No. 12174358, and No. 92265208), and NSAF (Grant No. U2330401).

APPENDIX A: DIAGONALIZATION OF HAMILTONIAN

In order to diagonalize the Hamiltonian $\hat{H}_0$ in Eq. (1), we choose the Wannier function of the dipole potential $V_d(x)$ as the basis and adopt the tight-binding approximation. By applying the Bloch theorem to Hamiltonian $\hat{H}_{\rm at}$ and expanding the Bloch wave function $|k\rangle$ in real space by the plane waves,

we get

$$\langle x|k\rangle \equiv \psi_k(x) = e^{ikx}u_k(x) = e^{ikx}\sum_{l=-l_c}^{+l_c} e^{i2lk_dx}u_k(l)\frac{1}{\sqrt{L}}$$
$$= \sum_{l=-l_c}^{+l_c}\frac{1}{\sqrt{L}}e^{i(k+2lk_d)x}u_k(l), \tag{A1}$$

where l_c is the cutoff of basis, $L = N\pi/k_d$ is the length of the system, and N is the number of dipolar lattice site. The quasimomentum $k \in [-k_d, +k_d)$ falls only in the first Brillouin zone with an interval $\Delta_k = 2k_d/N$. The expansion coefficient $u_k(l)$ can be obtained by diagonalizing Hamiltonian $\hat{H}_{\rm at}$ in the plane waves basis. After a shift of zero-point energy by $V_d/2$, the effective Hamiltonian $\hat{H}_{\rm at}(k)$ can be written as

$$\hat{H}_{\rm at}(k) = \begin{pmatrix} \frac{(k-2l_ck_d)^2}{2m} & \frac{V_d}{4} & \cdots & 0 & 0 \\ \frac{V_d}{4} & \frac{(k-2(l_c-1)k_d)^2}{2m} & \cdots & 0 & 0 \\ \vdots & \vdots & \ddots & \cdots & \cdots \\ 0 & 0 & \vdots & \frac{(k+2(l_c-1)k_d)^2}{2m} & \frac{V_d}{4} \\ 0 & 0 & \vdots & \frac{V_d}{4} & \frac{(k+2l_ck_d)^2}{2m} \end{pmatrix}, \tag{A2}$$

where the matrix elements $H_{\rm at}^{l,l'}(k)$ read

$$H_{\rm at}^{l,l'}(k) = \frac{1}{L}\int_{-\frac{L}{2}}^{\frac{L}{2}} e^{-i(k+2lk_d)x}\hat{H}_{\rm at}e^{i(k+2l'k_d)x}dx. \tag{A3}$$

We then take the single-band approximation and denote the Bloch states of the bottom band as $\psi_k(x)$. Here, we drop the band index to simplify notation.

The Wannier function $|j\rangle$ in real space can be obtained by Fourier transformation as

$$\langle x|j\rangle \equiv \phi_{R_j}(x) = \frac{1}{\sqrt{N}}\sum_k e^{-ikR_j}\psi_k(x), \tag{A4}$$

where $\{R_j\}$ is a set of discrete site positions. Further, the fermionic field operator can be expanded by the Wannier basis $\hat{\Psi}(x) = \sum_j \phi_{R_j}(x)\hat{c}_j$, where $\hat{c}_j$ is the fermionic annihilation operator at position j. With that, we obtain the Hamiltonian in the tight-binding approximation

$$\hat{H} = -t\sum_{\langle i,j\rangle}\hat{c}_i^\dagger\hat{c}_j + \eta(\hat{a}+\hat{a}^\dagger)\sum_i\cos(k_cR_i)\hat{c}_i^\dagger\hat{c}_i + \frac{U}{2}\hat{a}^\dagger\hat{a}\sum_i\cos(2k_cR_i)\hat{c}_i^\dagger\hat{c}_i - \delta_c\hat{a}^\dagger\hat{a}, \tag{A5}$$

where $\delta_c = \Delta_c - U_0N_{\rm at}/2$ and $N_{\rm at}$ is the atom number. Here, the nearest-neighbor hopping strength t and the renormalized parameters η and U are

$$t = -\int_{-\frac{L}{2}}^{\frac{L}{2}}\phi_{R_{i+1}}^*(x)\hat{H}_{\rm at}\phi_{R_i}(x)dx, \tag{A6}$$

$$\eta = \eta_0\int_{-\frac{L}{2}}^{\frac{L}{2}}|\phi_{R_i}(x)|^2\cos[k_c(x-R_i)]dx, \tag{A7}$$

$$U = U_0\int_{-\frac{L}{2}}^{\frac{L}{2}}|\phi_{R_i}(x)|^2\cos[2k_c(x-R_i)]dx. \tag{A8}$$

In Table I, we list the numerical results of t, η, and U for some typical choices of lattice depth V_d/E_R with E_R the recoil energy.

Finally, we employ the mean field approximation for the cavity mode $\langle\hat{a}\rangle = \alpha$ and write down the Hamiltonian

$$\hat{H}(\alpha) = -t\sum_{\langle i,j\rangle}\hat{c}_i^\dagger\hat{c}_j + \eta(\alpha+\alpha^*)\sum_i\cos(k_cR_i)\hat{c}_i^\dagger\hat{c}_i + \frac{U}{2}\alpha^*\alpha\sum_i\cos(2k_cR_i)\hat{c}_i^\dagger\hat{c}_i - \delta_c\alpha^*\alpha, \tag{A9}$$

from which the single-particle spectrum $\{\varepsilon_{n,\alpha}\}$ and the corresponding eigenstates $\{|\phi_{n,\alpha}\rangle\}$ can be calculated by diagonalizing Eq. (A9) under open boundary condition.

Before concluding this section, we stress that in our previous discussion, a fixed phase of the cavity mode α is assumed for simplicity, which is valid under the condition $\Delta_c \gg U_0\mathcal{B}$. To verify this assumption, we plot in Fig. 5 the ratio $|U_0\mathcal{B}/\Delta_c|$. This quantity remains to be less than 5% for different filling when $|\alpha| < 0.6$, validating the assumption of a fixed phase in all parameter regions discussed in this work.

TABLE I. Numerical results of t, η, and U for different lattice depths.

V_d/E_R	$4t/E_R$	η/η_0	U/U_0
3	0.444 109	0.909 491	0.855 470
5	0.263 069	0.938 906	0.892 875
10	0.076 730	0.962 952	0.930 528
15	0.026 075	0.971 324	0.945 272
20	0.009 965	0.975 816	0.953 465

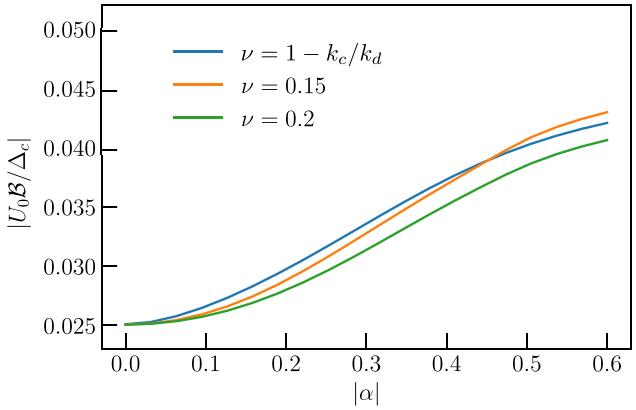

FIG. 5. Numerical results of $|U_0\mathcal{B}/\Delta_c|$ as a function of cavity mode $|\alpha|$ at different filling ν. Here, we use $V_d/E_R = 3$, $\eta_0/E_R = -0.273$, $U_0/E_R = -0.01$, $\Delta_c/E_R N_{\rm at} = -0.155$, $\kappa/E_R N_{at} = 0.0075$, and system size $N = 4000$.

APPENDIX B: FINITE SIZE ANALYSIS

1. $\mathcal{Z}_2$ symmetry of cavity mode

Owing to the incommensurability of k_c/k_d, one in general cannot assume *a priori* a $\mathcal{Z}_2$ symmetry of the cavity mode, in particular, for a finite-size system. To clarify this issue, we define the imbalance of energy at α and $-\alpha$ as

$$\frac{\Delta_\alpha}{E_R} = \frac{1}{E_R n_{\max}} \sum_{n=1}^{n_{\max}} |\varepsilon_n(\alpha) - \varepsilon_n(-\alpha)|, \tag{B1}$$

where $n_{\max}$ is the total number of energy levels under consideration. In Fig. 6, we show the numerical result of Δ_α/E_R by varying α and N. Indeed, we find a nonzero Δ_α/E_R for a finite-size system with $\alpha > 0$. However, the energy imbalance

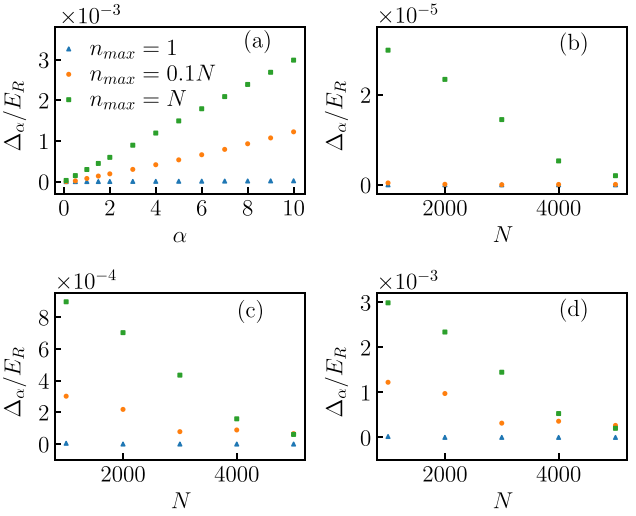

FIG. 6. (a) The energy imbalance Δ_α/E_R as a function of α for different $n_{\max}$ with $N = 1000$. (b–d) The energy imbalance Δ_α as a function of system size N for $\alpha = 0.1, 3$, and 10, respectively. Parameters used here are $V_d/E_R = 3$, $\eta_0/E_R = -0.273$, and $U_0/E_R = -0.01$, and α is assumed to be real.

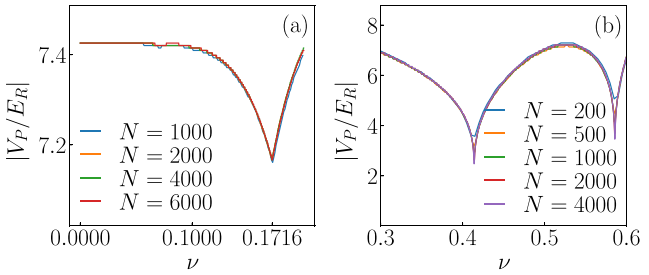

FIG. 7. The phase diagram around (a) the IRM filling and (b) the nesting filling for different size N. Parameters used here are $V_d/E_R = 3$, $U_0/E_R = -0.01$, $\Delta_c/E_R N_{\rm at} = -0.155$, and $\kappa/E_R N_{at} = 0.0075$.

is quite small for a large enough system with $\alpha \lesssim 1$, which is the case of particular interest in this work.

2. Phase diagram

In this section, we provide the finite size scaling of the phase diagram. Firstly, we analyze the dip around the IRM filling $\nu_{\rm IRM} = 1 - k_c/k_d$, at which a first-order Dicke transition takes place. As shown in Fig. 7(a), the phase boundary for systems of different size converge and the dip has a finite critical pumping strength $\eta_0/E_R \approx 0.268$. For systems with nesting filling, i.e., $\nu = k_c/2k_d$ and $1 - k_c/2k_d$, the superradiant transition is of second order. As shown in Fig. 7(b), the phase boundary for systems of different size converge almost everywhere except at the nesting filling. By increasing the precision of α and the size N, we find that the critical pumping strength tends to zero as shown in Fig. 8.

APPENDIX C: INVERSE PARTICIPATION RATIO

For a given eigenstate $\varphi_n(\alpha)$, we can define the single-state IPR as

$$\mathrm{IPR}^{(n)}(\alpha) = \frac{\sum_j |\langle j|\varphi_n(\alpha)\rangle|^4}{(\sum_j |\langle j|\varphi_n(\alpha)\rangle|^2)^2}. \tag{C1}$$

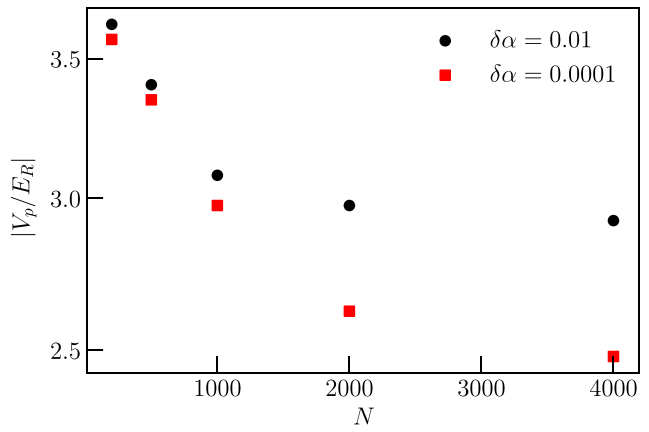

FIG. 8. The transition point at the nesting filling $\nu = k_c/2k_d$ for different system size N. The black circles and the red squares denote results of different precisions of α. Parameters used here are $V_d/E_R = 3$, $U_0/E_R = -0.01$, $\Delta_c/E_R N_{\rm at} = -0.155$, and $\kappa/E_R N_{at} = 0.0075$.

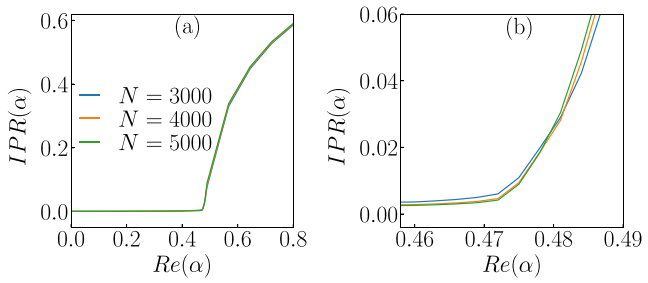

FIG. 9. (a) The mean inverse participation ratio IPR(α) as a function of Re(α) for different system size N. (b) A zoom-in of (a) showing the intersection of curves. The parameters are $V_d/E_R = 3$, $\eta_0/E_R = -0.273$, $U_0/E_R = -0.01$, $\Delta_c/E_R N_{\rm at} = -0.155$, and $\kappa/E_R N_{at} = 0.0075$.

For a spatially extended state $\mathrm{IPR}^{(n)}(\alpha)$ tends to zero, while for a localized state it approaches unity. In Fig. 2(a), we show the result of $\mathrm{IPR}^{(n)}(\alpha)$ for all single-particle eigenstates in false color.

By averaging over all eigenstates, we can define the mean inverse participation ratio for the total spectrum

$$\mathrm{IPR}(\alpha) = \frac{1}{N}\sum_n \mathrm{IPR}^{(n)}(\alpha), \tag{C2}$$

which can be used to distinguish localized phase and extended phase. Specifically, for a given pumping strength η_0, we calculate IPR(α) as a function of α for systems with different size, as shown in Fig. 9. The critical α of the localized–extended phase transition is determined by the average of intersection of curves for different sizes. Then, we vary η_0 and choose the largest α to plot the Anderson localization transition line (dash-dotted) in Fig. 4(c).

APPENDIX D: PHENOMENOLOGICAL THEORY

In this section, we will derive a phenomenological DOS and calculate the effective ground-state energy density

$$E_g(\alpha) = E_{\rm vac}(\alpha) + E_{\rm occ}(\alpha), \tag{D1}$$

where $E_{\rm vac}(\alpha)$ is the single-particle ground-state energy shift, or vacuum energy in brief, and $E_{\rm occ}(\alpha)$ is the occupation energy by filling the states below the Fermi level. The occupation energy can be written as

$$E_{\rm occ}(\alpha) = \int d\varepsilon D_\alpha(\varepsilon)\varepsilon, \tag{D2}$$

with $D_\alpha(\varepsilon)$ the DOS. In the following discussion, we take $\kappa = 0$ and assume α is real for simplicity.

1. Direct resonance at nesting filling

We first study the direct resonance at nesting filling when $k_F = k_c/2$. To describe the van Hove singularity at the band edge, we assume an approximate dispersion

$$\varepsilon = \tilde{\varepsilon}_{\rm N} - \sqrt{\left(\frac{k^2}{2m^*} - \tilde{\varepsilon}_{\rm N}\right)^2 + 4\eta^2\alpha^2} \tag{D3}$$

for the bottom band below nesting energy $\tilde{\varepsilon}_{\rm N} = \varepsilon_{k_c/2}$, where m^* is the effective mass considering the lattice correction, and $2|\eta\alpha|$ is the resonance-induced gap. We stress that this simple form of dispersion can correctly capture the diverging characteristics at band edges, which are crucial to determine the critical behavior of the superradiant phase transition around the resonance point. The DOS can then be written as

$$D_\alpha(\varepsilon) = \frac{D_0}{\sqrt{\tilde{\varepsilon}_{\rm N} - \sqrt{\Delta\varepsilon^2 - 4\eta^2\alpha^2}}} \frac{|\Delta\varepsilon|}{\sqrt{\Delta\varepsilon^2 - 4\eta^2\alpha^2}}, \tag{D4}$$

where $\Delta\varepsilon \equiv \varepsilon - \tilde{\varepsilon}_{\rm N}$, and D_0 is a constant determined by the constraint of particle number $N_0 = \int d\varepsilon D_\alpha(\varepsilon)$. Indeed, we can easily find that

$$\begin{aligned} N_0 &= \int_{\tilde{\varepsilon}_{\rm N}-\sqrt{\tilde{\varepsilon}_{\rm N}^2+4\eta^2\alpha^2}}^{\tilde{\varepsilon}_{\rm N}-2\eta\alpha} d\varepsilon \frac{D_0}{\sqrt{\tilde{\varepsilon}_{\rm N} - \sqrt{\Delta\varepsilon^2 - 4\eta^2\alpha^2}}} \\ &\quad \times \frac{|\Delta\varepsilon|}{\sqrt{\Delta\varepsilon^2 - 4\eta^2\alpha^2}} \\ &= D_0\sqrt{2\eta\alpha}\int_1^{\frac{\sqrt{\tilde{\varepsilon}_{\rm N}^2+4\eta^2\alpha^2}}{2\eta\alpha}} dx \frac{1}{\sqrt{\frac{\tilde{\varepsilon}_{\rm N}}{2\eta\alpha} - \sqrt{x^2-1}}} \frac{x}{\sqrt{x^2-1}} \\ &= D_0\sqrt{2\eta\alpha}\int_0^{\arccos\frac{2\eta\alpha}{\sqrt{\tilde{\varepsilon}_{\rm N}^2+4\eta^2\alpha^2}}} \frac{d\theta}{\cos^2\theta} \frac{1}{\sqrt{\frac{\tilde{\varepsilon}_{\rm N}}{2\eta\alpha} - \tan\theta}} \\ &= D_0\sqrt{2\eta\alpha}\int_0^{\frac{\tilde{\varepsilon}_{\rm N}}{2\eta\alpha}} \frac{dy}{\sqrt{\frac{\tilde{\varepsilon}_{\rm N}}{2\eta\alpha} - y}} = 2D_0\sqrt{\tilde{\varepsilon}_{\rm N}}, \end{aligned} \tag{D5}$$

i.e., $D_0 = N_0/2\sqrt{\tilde{\varepsilon}_{\rm N}}$ is a constant independent of α.

For a system with a filling ν slightly lower than the nesting filling $\nu_{\rm N}$, the number constraint reads

$$\begin{aligned} \frac{N_0\nu}{\nu_{\rm N}} &= \int_{\tilde{\varepsilon}_{\rm N}-\sqrt{\tilde{\varepsilon}_{\rm N}^2+4\eta^2\alpha^2}}^{\mu} d\varepsilon D_\alpha(\varepsilon) \\ &= D_0\sqrt{2\eta\alpha}\int_{\frac{\sqrt{(\tilde{\varepsilon}_{\rm N}-\mu)^2-4\eta^2\alpha^2}}{2\eta\alpha}}^{\frac{\tilde{\varepsilon}_{\rm N}}{2\eta\alpha}} \frac{dy}{\sqrt{\frac{\tilde{\varepsilon}_{\rm N}}{2\eta\alpha} - y}}, \end{aligned} \tag{D6}$$

from which we can obtain the chemical potential

$$\mu = \tilde{\varepsilon}_{\rm N} - \sqrt{\left[1 - \left(\frac{\nu}{\nu_{\rm N}}\right)^2\right]^2 \tilde{\varepsilon}_{\rm N}^2 + 4\eta^2\alpha^2}. \tag{D7}$$

The occupation energy then becomes

$$\begin{aligned} E_{\rm occ}(\alpha) &= \int_{\tilde{\varepsilon}_{\rm N}-\sqrt{\tilde{\varepsilon}_{\rm N}^2+4\eta^2\alpha^2}}^{\mu} d\varepsilon\varepsilon D_\alpha(\varepsilon) \\ &= \int_{\tilde{\varepsilon}_{\rm N}-\mu}^{\sqrt{\tilde{\varepsilon}_{\rm N}^2+4\eta^2\alpha^2}} d\varepsilon(\tilde{\varepsilon}_{\rm N} - \varepsilon) D_\alpha(\tilde{\varepsilon}_{\rm N} - \varepsilon). \end{aligned} \tag{D8}$$

Under the condition $1-\nu/\nu_{\rm N}\to 0$, it is easy to obtain

$$\begin{aligned} &N_0\tilde{\varepsilon}_{\rm N}-E_{\rm occ}(\alpha)\\ &=\int_{\tilde{\varepsilon}_{\rm N}-\mu}^{\sqrt{\tilde{\varepsilon}_{\rm N}^2+4\eta^2\alpha^2}} d\varepsilon \frac{D_0}{\sqrt{\tilde{\varepsilon}_{\rm N}-\sqrt{\varepsilon^2-4\eta^2\alpha^2}}}\frac{\varepsilon^2}{\sqrt{\varepsilon^2-4\eta^2\alpha^2}}\\ &=D_0(2\eta\alpha)^{3/2}\int_{\frac{\tilde{\varepsilon}_{\rm N}-\mu}{2\eta\alpha}}^{\frac{\sqrt{\tilde{\varepsilon}_{\rm N}^2+4\eta^2\alpha^2}}{2\eta\alpha}} \frac{dx}{\sqrt{\frac{\tilde{\varepsilon}_{\rm N}}{2\eta\alpha}-\sqrt{x^2-1}}}\frac{x^2}{\sqrt{x^2-1}}\\ &=D_0(2\eta\alpha)^{3/2}\int_{\frac{\sqrt{(\tilde{\varepsilon}_{\rm N}-\mu)^2-4\eta^2\alpha^2}}{2\eta\alpha}}^{\frac{\tilde{\varepsilon}_{\rm N}}{2\eta\alpha}} dy\frac{\sqrt{1+y^2}}{\sqrt{\frac{\tilde{\varepsilon}_{\rm N}}{2\eta\alpha}-y}}. \end{aligned} \tag{D9}$$

By defining $y\equiv\frac{\tilde{\varepsilon}_{\rm N}}{2\eta\alpha}\sin^2\phi$, we have

$$\begin{aligned} &N_0\tilde{\varepsilon}_{\rm N}-E_{\rm occ}(\alpha)\\ &=N_0\tilde{\varepsilon}_{\rm N}\int_{\arcsin\sqrt{\frac{\sqrt{(\tilde{\varepsilon}_{\rm N}-\mu)^2-4\eta^2\alpha^2}}{\tilde{\varepsilon}_{\rm N}}}}^{\frac{\pi}{2}} d\phi\sin\phi\sqrt{\sin^4\phi+\frac{4\eta^2\alpha^2}{\tilde{\varepsilon}_{\rm N}^2}}\\ &\approx N_0\tilde{\varepsilon}_{\rm N}\int_{\sqrt{2(1-\nu/\nu_{\rm N})}}^{\frac{\pi}{2}} d\phi\sin\phi\sqrt{\sin^4\phi+\frac{4\eta^2\alpha^2}{\tilde{\varepsilon}_{\rm N}^2}}, \end{aligned} \tag{D10}$$

where the expression of chemical potential Eq. (D7) is substituted. Finally, we obtain

$$\begin{aligned} E_{\rm occ}(\alpha)&=N_0\tilde{\varepsilon}_{\rm N}-N_0\tilde{\varepsilon}_{\rm N}\int_{\sqrt{2(1-\nu/\nu_{\rm N})}}^{\frac{\pi}{2}} d\phi\sin\phi\sqrt{\sin^4\phi+\frac{4\eta^2\alpha^2}{\tilde{\varepsilon}_{\rm N}^2}}\\ &\approx N_0\tilde{\varepsilon}_{\rm N}-N_0\tilde{\varepsilon}_{\rm N}\int_{\tilde{\nu}_{\rm N}}^{1} dx\sqrt{x^2(2-x)^2+\frac{4\eta^2\alpha^2}{\tilde{\varepsilon}_{\rm N}^2}} \end{aligned} \tag{D11}$$

with $\tilde{\nu}_{\rm N}\equiv 1-\nu/\nu_{\rm N}$. Notice that the first term on the right-hand side is a constant and can be dropped out as a zero-point energy. Then we get the expression used in Eq. (8).

For a system with filling slightly higher than the nesting filling, an analogous derivation leads to a similar result as Eq. (D11) with the lower bound of the integral changing to $\nu/\nu_{\rm N}-1$.

2. Indirect resonance modulation at IRM filling

Following a similar derivation as in the previous section, we can get the ground-state energy $E_g(\alpha)$ around the IRM filling $\nu_{\rm IRM}$ analogous to Eq. (D11),

$$E_g(\alpha)=E_{\rm vac}(\alpha)-N_0'\tilde{\varepsilon}_{\rm R}\int_{\tilde{\nu}_{\rm IRM}}^{1} dx\sqrt{x^2(2-x)^2+\frac{\Delta_{\rm IRM}^2(\alpha)}{\tilde{\varepsilon}_{\rm R}^2}}, \tag{D12}$$

with $E_{\rm vac}(\alpha)=(1-\tilde{\nu}_{\rm IRM})N_0'\varepsilon_{0,\alpha}-\Delta_c\alpha^2$, $\tilde{\varepsilon}_{\rm R}=\sqrt{\tilde{\varepsilon}_{\rm N}^2+4\eta^2\alpha^2}-\sqrt{(\tilde{\varepsilon}_{\rm N}-\tilde{\varepsilon}_{\rm IRM})^2+4\eta^2\alpha^2}$, and $\tilde{\nu}_{\rm IRM}\equiv 1-\nu/\nu_{\rm IRM}$. The gap of the single-particle dispersion $\Delta_{\rm IRM}$ depends on α quadratically for small α. This behavior is in stark contrast to the case of nesting filling where a linear dependence is found. The prefactor of the α^2 term in E_g remains positive when α is small, and the superradiant transition can only take place at a finite α.

To analyze the superradiant transition around the IRM filling, we denote the critical pumping strength as η_0 and the critical cavity field as α_c for a specific value of $\tilde{\nu}_{\rm IRM}=\tilde{\nu}_0$. Since the phase transition is of first order, we have

$$E_g(\tilde{\nu}_0,\alpha=0,\eta_0)=E_g(\tilde{\nu}_0,\alpha=\alpha_c,\eta_0). \tag{D13}$$

Next, we consider an increment of filling $\tilde{\nu}_{\rm IRM}\to\tilde{\nu}_0+\delta\tilde{\nu}$, and denote the corresponding critical pumping strength as $\eta_0+\delta\eta$ and critical cavity field as $\alpha_c+\delta\alpha$. The condition of phase transition then reads

$$\begin{aligned} &E_g(\tilde{\nu}_0+\delta\tilde{\nu},\alpha=\delta\alpha,\eta_0+\delta\eta)\\ &\quad=E_g(\tilde{\nu}_0+\delta\tilde{\nu},\alpha=\alpha_c+\delta\alpha,\eta_0+\delta\eta). \end{aligned} \tag{D14}$$

Expanding the expression above to linear order of $\delta\tilde{\nu}$, $\delta\eta$, and $\delta\alpha$, we can easily conclude that the critical pumping field is linearly dependent on filling with

$$\frac{\delta\eta}{\delta\tilde{\nu}}=\frac{\zeta_1\zeta_6-\zeta_3\zeta_4}{\zeta_3\zeta_5-\zeta_2\zeta_6}, \tag{D15}$$

where

$$\begin{aligned} \zeta_1&=\frac{1}{N_0'}\frac{\partial[E_{\rm vac}(\tilde{\nu},\alpha=0,\eta_0)-E_{\rm vac}(\tilde{\nu},\alpha=\alpha_c,\eta_0)]}{\partial\tilde{\nu}}\bigg|_{\tilde{\nu}=\tilde{\nu}_0}\\ &\quad+[T(\tilde{\nu}_0,\alpha=0,\eta_0)-T(\tilde{\nu}_0,\alpha=\alpha,\eta_0)],\\ \zeta_2&=\frac{1}{N_0'}\frac{\partial[E_{\rm vac}(\tilde{\nu}_0,\alpha=0,\eta)-E_{\rm vac}(\tilde{\nu}_0,\alpha=\alpha_c,\eta)]}{\partial\eta}\bigg|_{\eta=\eta_0}\\ &\quad-\int_{\tilde{\nu}_0}^{1}dx\frac{\partial[T(x,\alpha=0,\eta)-T(x,\alpha=\alpha_c,\eta)]}{\partial\eta}\bigg|_{\eta=\eta_0},\\ \zeta_3&=\frac{1}{N_0'}\left[\frac{\partial E_{\rm vac}(\tilde{\nu}_0,\alpha,\eta_0)}{\partial\alpha}\bigg|_{\alpha=\alpha_c}-\frac{\partial E_{\rm vac}(\tilde{\nu}_0,\alpha,\eta_0)}{\partial\alpha}\bigg|_{\alpha=0}\right]\\ &\quad-\int_{\tilde{\nu}_0}^{1}dx\left[\frac{\partial T(x,\alpha,\eta_0)}{\partial\alpha}\bigg|_{\alpha=\alpha_c}-\frac{\partial T(x,\alpha,\eta_0)}{\partial\alpha}\bigg|_{\alpha=0}\right],\\ \zeta_4&=\frac{1}{N_0'}\frac{\partial^2E_{\rm vac}(\tilde{\nu},\alpha,\eta_0)}{\partial\alpha\partial\tilde{\nu}}\bigg|_{\tilde{\nu}=\tilde{\nu}_0,\alpha=\alpha_c}+\frac{\partial T(\tilde{\nu}_0,\alpha,\eta_0)}{\partial\alpha}\bigg|_{\alpha=\alpha_c},\\ \zeta_5&=\frac{1}{N_0'}\frac{\partial^2E_{\rm vac}(\tilde{\nu}_0,\alpha,\eta)}{\partial\alpha\partial\eta}\bigg|_{\eta=\eta_0,\alpha=\alpha_c}\\ &\quad-\int_{\tilde{\nu}_0}^{1}dx\frac{\partial^2T(x,\alpha,\eta)}{\partial\alpha\partial\eta}\bigg|_{\eta=\eta_0,\alpha=\alpha_c},\\ \zeta_6&=-\frac{1}{N_0'}\frac{\partial^2E_{\rm vac}(\tilde{\nu}_0,\alpha,\eta_0)}{\partial\alpha^2}\bigg|_{\alpha=\alpha_c}\\ &\quad+\int_{\tilde{\nu}_0}^{1}dx\frac{\partial^2T(x,\alpha,\eta_0)}{\partial\alpha^2}\bigg|_{\alpha=\alpha_c}. \end{aligned} \tag{D16}$$

and

$$T(x,\alpha,\eta)=\sqrt{x^2(2-x)^2+\frac{\Delta_{\rm IRM}^2(\alpha)}{\tilde{\varepsilon}_{\rm R}^2}}. \tag{D17}$$

The linear dependence Eq. (D15) of the critical pumping strength on filling can be numerically verified, as shown in Fig. 10.

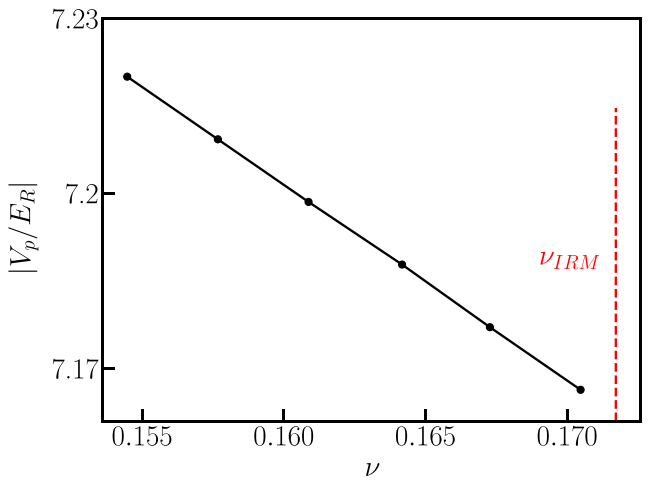

FIG. 10. The critical pumping η_0/E_R as a function of filling ν near the IRM filling. Parameters used are $V_d/E_R = 3$, $U_0/E_R = -0.01$, $\Delta_c/E_R N_{\rm at} = -0.1774$, and $N = 4000$.

APPENDIX E: EFFECTIVE THEORY BETWEEN $\nu_{\rm IRM}$ AND $\nu_{\rm N}$

The phenomenological theory is based on the effective DOS as a function of α. Within the region above the indirect resonance filling $\nu_{\rm IRM}$ and below the nesting filling $\nu_{\rm N}$, we assume the following form:

$$D''_\alpha(\varepsilon) = \frac{D''_0|\Delta\varepsilon''|}{\sqrt{\Delta\varepsilon''^2 - \Delta^2_{\rm IRM}(\alpha)}} \frac{|\Delta\varepsilon|}{\sqrt{\Delta\varepsilon^2 - 4\eta^2\alpha^2}}, \tag{E1}$$

where $\Delta\varepsilon'' = \varepsilon - \tilde{\varepsilon}_d$, $\Delta\varepsilon = \varepsilon - \tilde{\varepsilon}_u$, and $\tilde{\varepsilon}_d = \tilde{\varepsilon}_{\rm N} - \sqrt{(\varepsilon_{\rm N} - \varepsilon_{\rm IRM})^2 + 4\eta^2\alpha^2}$ and $\tilde{\varepsilon}_u = \tilde{\varepsilon}_{\rm N} + \Delta_{\rm IRM}$ are lower and upper bounds of the band edge, respectively.

The above DOS can be further approximated as

$$D_\alpha(\varepsilon) = \frac{D''_0|\Delta\varepsilon''|}{\sqrt{\Delta\varepsilon''^2 - \Delta^2_{\rm IRM}(\alpha)}}\Theta(\varepsilon_m - \varepsilon) + \frac{D''_0|\Delta\varepsilon|}{\sqrt{\Delta\varepsilon^2 - 4\eta^2\alpha^2}}\Theta(\varepsilon - \varepsilon_m), \tag{E2}$$

where $\varepsilon_m = (\tilde{\varepsilon}_u - 2|\eta\alpha| + \tilde{\varepsilon}_d + \Delta_{\rm IRM})/2$ is the middle between the upper bound and lower bound. By requiring $\int_{\tilde{\varepsilon}_d+\Delta_{\rm IRM}}^{\tilde{\varepsilon}_u-2\eta\alpha} D''_\alpha(\varepsilon)d\varepsilon = N_0 - N'_0$, we have

$$D''_0 = \frac{(1-\nu_{\rm IRM})N_0}{\sqrt{(\varepsilon_m - \tilde{\varepsilon}_d)^2 - \Delta^2_{\rm IRM}} + \sqrt{(\tilde{\varepsilon}_u - \varepsilon_m)^2 - 4\eta^2\alpha^2}}. \tag{E3}$$

With that, a simple relation can be obtained for the filling ν_m at a given energy ε_m,

$$\frac{\sqrt{(\tilde{\varepsilon}_m - \tilde{\varepsilon}_d)^2 - \Delta^2}}{\sqrt{(\varepsilon_m - \tilde{\varepsilon}_d)^2 - \Delta^2_{\rm IRM}} + \sqrt{(\tilde{\varepsilon}_u - \varepsilon_m)^2 - 4\eta^2\alpha^2}} = \frac{\nu_m - \nu_{\rm IRM}}{1-\nu_{\rm IRM}}. \tag{E4}$$

Then, we can determine the chemical potential μ as

$$\mu = \Theta(\nu_m - \nu)\left(\tilde{\varepsilon}_d + \sqrt{\left(\frac{(\nu-\nu_{\rm IRM})N_0/\nu_{\rm N}}{D''_0}\right)^2 + \Delta^2_{\rm IRM}}\right) + \Theta(\nu - \nu_{\rm IRM})\left(\tilde{\varepsilon}_u - \sqrt{\left(\frac{(1-\nu/\nu_{\rm N})N_0}{D''_0}\right)^2 + 4\eta^2\alpha^2}\right). \tag{E5}$$

For $\nu < \nu_m$, the extra occupation energy is $E'_{\rm occ}(\nu,\alpha) \equiv \int_{\tilde{\varepsilon}_d+\Delta_{\rm IRM}}^{\mu} D''_\alpha(\varepsilon)\varepsilon d\varepsilon$, leading to

$$\begin{aligned} E'_{\rm occ}(\nu,\alpha) &= \int_{\tilde{\varepsilon}_d+\Delta}^{\mu} d\varepsilon D_\alpha(\varepsilon)(\varepsilon - \varepsilon_{g0}) \\ &= (\tilde{\varepsilon}_d - \varepsilon_{g0})(\nu-\nu_{\rm IRM})N_0 + \int_{\Delta}^{\sqrt{(\frac{(\nu-\nu_{\rm IRM})N_0}{D''_0})^2+\Delta^2_{\rm IRM}}} dx \frac{x^2}{\sqrt{x^2 - \Delta^2_{\rm IRM}}}, \\ &= (\tilde{\varepsilon}_d - \varepsilon_{g0})(\nu-\nu_{\rm IRM})N_0 + \frac{1}{2}\left[\sqrt{\left(\frac{\tilde{\nu}_{\rm IRM}N_0}{D''_0}\right)^2 + \Delta^2_{\rm IRM}}\tilde{\nu}_{\rm IRM}N_0 + D''_0\Delta^2_{\rm IRM}\ln\frac{\sqrt{\left(\frac{\tilde{\nu}_{\rm IRM}N_0}{D''_0}\right)^2 + \Delta^2} + \frac{\tilde{\nu}_{\rm IRM}N_0}{D''_0}}{\Delta_{\rm IRM}}\right]. \end{aligned} \tag{E6}$$

For $\nu_m < \nu < \nu_{\rm N}$, we have

$$\begin{aligned} E'_{\rm occ}(\alpha,\nu) &= (\tilde{\varepsilon}_d - \varepsilon_{g0})\tilde{\nu}_{\rm IRM}N_0 + (\tilde{\varepsilon}_u - \varepsilon_d)(\nu-\nu_m)N_0/\nu_{\rm N} + \Theta(P_c - |\eta\alpha|)\frac{1}{2}\sqrt{\left(\frac{\tilde{\nu}_{md}N_0}{D''_0}\right)^2 + \Delta^2_{\rm IRM}}\tilde{\nu}_{md}N_0 \\ &+ \Theta(|\eta\alpha| - P_c)\frac{1}{2}\left[\sqrt{\left(\frac{\tilde{\nu}_{md}N_0}{D''_0}\right)^2 + \Delta^2_{\rm IRM}}\tilde{\nu}_{md}N_0 + D''_0\Delta^2_{\rm IRM}\ln\left(\sqrt{1 + \left(\frac{\tilde{\nu}_{md}N_0}{D''_0\Delta_{\rm IRM}}\right)^2} + \frac{\tilde{\nu}_{md}N_0}{D''_0\Delta_{\rm IRM}}\right)\right] \end{aligned}$$

$$-\frac{1}{2}\left[\sqrt{\left(\frac{\tilde{\nu}_{um}N_0}{D_0''}\right)^2+4\eta^2\alpha^2\tilde{\nu}_{um}N_0}+4D_0''\eta^2\alpha^2\ln\left(\sqrt{4\eta^2\alpha^2+\left(\frac{\tilde{\nu}_{um}N_0}{D_0''}\right)^2}+\frac{\tilde{\nu}_{um}N_0}{D_0''}\right)\right]$$

$$+\frac{1}{2}\left[\sqrt{\left(\frac{\tilde{\nu}N_0}{D_0''}\right)^2+4\eta^2\alpha^2\tilde{\nu}N_0}+4D_0''\eta^2\alpha^2\ln\left(\sqrt{4\eta^2\alpha^2+\left(\frac{\tilde{\nu}N_0}{D_0''}\right)^2}+\frac{\tilde{\nu}N_0}{D_0''}\right)\right], \tag{E7}$$

where P_c is typical indirect gap opening strength of $|\eta\alpha|$ [here we take $\Delta_{\mathrm{IRM}}\approx 0.2\Theta(|\eta\alpha|-P_c)(|\eta\alpha|-P_c)$], $\tilde{\nu}_{md}=(\nu_m-\nu_{\mathrm{IRM}})/\nu_{\mathrm{N}}$, $\tilde{\nu}_{um}=1-\nu_m/\nu_{\mathrm{N}}$, and $\tilde{\nu}=1-\nu/\nu_{\mathrm{N}}$. The total ground-state energy is then

$$E_g(\alpha)=E_g^{\mathrm{IR}}(\alpha)\big|_{\tilde{\nu}_{\mathrm{IRM}}=0}+E'_{\mathrm{occ}}(\alpha,\nu). \tag{E8}$$

From the results above, we can obtain the phase diagram shown in Fig. 4(d).

[1] D. Levine and P. J. Steinhardt, Quasicrystals: A new class of ordered structures, Phys. Rev. Lett. **53**, 2477 (1984).

[2] D. Shechtman, I. Blech, D. Gratias, and J. W. Cahn, Metallic phase with long-range orientational order and no translational symmetry, Phys. Rev. Lett. **53**, 1951 (1984).

[3] N. G. de Bruijn, Algebraic theory of Penroses non-periodic tilings of the plane. I, Indagationes Mathematicae (Proceedings) **84**, 39 (1981).

[4] N. G. de Bruijn, Algebraic theory of Penroses non-periodic tilings of the plane. II, Indagationes Mathematicae (Proceedings) **84**, 53 (1981).

[5] P. Kramer and R. Neri, On periodic and non-periodic space fillings of E^m obtained by projection, Acta Crystallogr. Sect. A **40**, 580 (1984).

[6] A. I. Goldman and R. F. Kelton, Quasicrystals and crystalline approximants, Rev. Mod. Phys. **65**, 213 (1993).

[7] W. Steurer, Quasicrystals: What do we know? What do we want to know? What can we know? Acta Crystallogr., Sect. A **74**, 1 (2018).

[8] C. Gross and I. Bloch, Quantum simulations with ultracold atoms in optical lattices, Science **357**, 995 (2017).

[9] K. Viebahn, M. Sbroscia, E. Carter, J.-C. Yu, and U. Schneider, Matter-wave diffraction from a quasicrystalline optical lattice, Phys. Rev. Lett. **122**, 110404 (2019).

[10] L. Sanchez-Palencia and L. Santos, Bose-Einstein condensates in optical quasicrystal lattices, Phys. Rev. A **72**, 053607 (2005).

[11] J. E. Lye, L. Fallani, C. Fort, V. Guarrera, M. Modugno, D. S. Wiersma, and M. Inguscio, Effect of interactions on the localization of a Bose-Einstein condensate in a quasiperiodic lattice, Phys. Rev. A **75**, 061603(R) (2007).

[12] A. Cetoli and E. Lundh, Loss of coherence and superfluid depletion in an optical quasicrystal, J. Phys. B **46**, 085302 (2013).

[13] A. Jagannathan and M. Duneau, An eightfold optical quasicrystal with cold atoms, Europhys. Lett. **104**, 66003 (2013).

[14] P. Bordia, H. Lüschen, S. Scherg, S. Gopalakrishnan, M. Knap, U. Schneider, and I. Bloch, Probing slow relaxation and many-body localization in two-dimensional quasiperiodic systems, Phys. Rev. X **7**, 041047 (2017).

[15] S. Spurrier and N. R. Cooper, Semiclassical dynamics, Berry curvature, and spiral holonomy in optical quasicrystals, Phys. Rev. A **97**, 043603 (2018).

[16] J. Hou, H. Hu, K. Sun, and C. Zhang, Superfluid-quasicrystal in a Bose-Einstein condensate, Phys. Rev. Lett. **120**, 060407 (2018).

[17] F. Brennecke, T. Donner, S. Ritter, T. Bourdel, M. Köhl, and T. Esslinger, Cavity QED with a Bose-Einstein condensate, Nature (London) **450**, 268 (2007).

[18] K. Baumann, C. Guerlin, F. Brennecke, and T. Esslinger, Dicke quantum phase transition with a superfluid gas in an optical cavity, Nature (London) **464**, 1301 (2010).

[19] K. Baumann, R. Mottl, F. Brennecke, and T. Esslinger, Exploring symmetry breaking at the Dicke quantum phase transition, Phys. Rev. Lett. **107**, 140402 (2011).

[20] R. Mottl, F. Brennecke, K. Baumann, R. Landig, T. Donner, and T. Esslinger, Roton-type mode softening in a quantum gas with cavity-mediated long-range interactions, Science **336**, 1570 (2012).

[21] R. Landig, F. Brennecke, R. Mottl, T. Donner, and T. Esslinger, Measuring the dynamic structure factor of a quantum gas undergoing a structural phase transition, Nat. Commun. **6**, 7046 (2015).

[22] H. Ritsch, P. Domokos, F. Brennecke, and T. Esslinger, Cold atoms in cavity-generated dynamical optical potentials, Rev. Mod. Phys. **85**, 553 (2013).

[23] F. Mivehvar, F. Piazza, T. Donner, and H. Ritsch, Cavity QED with quantum gases: New paradigms in many-body physics, Adv. Phys. **70**, 1 (2021).

[24] W. Zheng and N. R. Cooper, Anomalous diffusion in a dynamical optical lattice, Phys. Rev. A **97**, 021601(R) (2018).

[25] H. Yin, J. Hu, A.-C. Ji, G. Juzeliūnas, X.-J. Liu, and Q. Sun, Localization driven superradiant instability, Phys. Rev. Lett. **124**, 113601 (2020).

[26] F. Mivehvar, H. Ritsch, and F. Piazza, Emergent quasicrystalline symmetry in light-induced quantum phase transitions, Phys. Rev. Lett. **123**, 210604 (2019).

[27] J. Keeling, M. J. Bhaseen, and B. D. Simons, Fermionic superradiance in a transversely pumped optical cavity, Phys. Rev. Lett. **112**, 143002 (2014).

[28] F. Piazza and P. Strack, Umklapp Superradiance with a collisionless quantum degenerate Fermi gas, Phys. Rev. Lett. **112**, 143003 (2014).

[29] Y. Chen, Z. Yu, and H. Zhai, Superradiance of degenerate Fermi gases in a cavity, Phys. Rev. Lett. **112**, 143004 (2014).

[30] X. Zhang, Y. Chen, Z. Wu, J. Wang, J. Fan, S. Deng, and H. Wu, Observation of a superradiant quantum phase transition in an intracavity degenerate Fermi gas, Science **373**, 1359 (2021).

[31] V. Helson, T. Zwettler, F. Mivehvar, E. Colella, K. Roux, H. Konishi, H. Ritsch, and J.-P. Brantut, Density-wave ordering in a unitary Fermi gas with photon-mediated interactions, Nature (London) **618**, 716 (2023).

[32] A. B. Deb and N. Kjærgaard, Observation of Pauli blocking in light scattering from quantum degenerate fermions, Science **374**, 972 (2021).

[33] Y. Margalit, Y.-K. Lu, F. Ç. Top, and W. Ketterle, Pauli blocking of light scattering in degenerate fermions, Science **374**, 976 (2021).

[34] C. Sanner, L. Sonderhouse, R. B. Hutson, L. Yan, W. R. Milner, and J. Ye, Pauli blocking of atom-light scattering, Science **374**, 979 (2021).

[35] N. F. Mott, On the transition to metallic conduction in semiconductors, Can. J. Phys. **34**, 1356 (1956).

[36] N. F. Mott, Conduction in non-crystalline materials, Philos. Mag. **19**, 835 (1969).

[37] N. F. Mott and E. A. Davis, *Electronic Processes in Non-Crystalline Materials* (Oxford University Press, New York, 1979).

[38] F. Piazza and P. Strack, Quantum kinetics of ultracold fermions coupled to an optical resonator, Phys. Rev. A **90**, 043823 (2014).